INTERNATIONAL JOURNAL FOR NUMERICAL METHODS IN FLUIDS
Int. J. Numer. Meth. Fluids 2003; **41**:721–741 (DOI: 10.1002/fld.468)

Potential flow around obstacles using the scaled boundary finite-element method

Andrew J. Deeks*,† and Liang Cheng

Department of Civil and Resource Engineering, The University of Western Australia, Crawley, Western Australia 6009, Australia

SUMMARY

The scaled boundary finite-element method is a novel semi-analytical technique, combining the advantages of the finite element and the boundary element methods with unique properties of its own. The method works by weakening the governing differential equations in one co-ordinate direction through the introduction of shape functions, then solving the weakened equations analytically in the other (radial) co-ordinate direction. These co-ordinate directions are defined by the geometry of the domain and a scaling centre. The method can be employed for both bounded and unbounded domains. This paper applies the method to problems of potential flow around streamlined and bluff obstacles in an infinite domain. The method is derived using a weighted residual approach and extended to include the necessary velocity boundary conditions at infinity. The ability of the method to model unbounded problems is demonstrated, together with its ability to model singular points in the near field in the case of bluff obstacles. Flow fields around circular and square cylinders are computed, graphically illustrating the accuracy of the technique, and two further practical examples are also presented. Comparisons are made with boundary element and finite difference solutions. Copyright © 2003 John Wiley & Sons, Ltd.

KEY WORDS: scaled boundary finite-element method; Laplace's equation; potential flow; unbounded domains; singular points

1. INTRODUCTION

The scaled boundary finite-element method is a novel and semi-analytical approach to the solution of partial differential equations developed by Wolf and Song. Until recently the method has mainly been used for the solution of problems of elasto-statics and elasto-dynamics. The method was originally derived to compute the dynamic stiffness of an unbounded domain [1],

*Correspondence to: A. J. Deeks, Department of Civil and Resource Engineering, The University of Western Australia, Crawley, Western Australia 6009, Australia.
†E-mail: deeks@civil.uwa.edu.au

Received January 2002
Accepted 16 October 2002

using a 'cloning' technique in which the analytical limit is taken as the width of the cloned finite-element cell tends to zero. The method proved to be more general than initially envisaged, with later developments allowing analysis of incompressible material and bounded domains [2], and the inclusion of body loads [3]. The complexity of the original derivation of the technique led to the development of a weighted residual formulation [4, 5], and recently a simplified virtual work derivation for elastostatics [6, 7].

Formulation of the method for solution of a two-dimensional scalar wave equation is available in [2], and has been applied to the problem of diffusion in an unbounded medium [8]. Neglecting the time-varying terms leads to the Laplace equation. However, so far only problems involving the out-of-plane motion of a wedge have been addressed by solution of the Laplace equation in this way [3, 9].

Although potential flow situations may be addressed by finite element and finite difference methods, problems involving the perturbation of a uniform flow of infinite extent by an obstacle are often solved by boundary element methods, as this overcomes the need to artificially truncate the solution domain in some way. Boundary element methods most commonly obtain an approximate solution for the velocity potential. However, in practical applications the velocity is often the most important characteristic of the flow, and must then be obtained from the potential field by some type of numerical differentiation. An alternative boundary element approach [10] can be used to obtain the velocity field directly. Obstacles with sharp corners cause additional problems, as the velocity is in general singular at the corners. To obtain accurate results using the boundary element method, *a priori* knowledge of the form of the singularities can be used to allow their removal from the boundary element solution process [11].

The scaled boundary finite-element method has several features that make it ideal for solving problems of potential flow around obstacles. The unbounded domain can be handled accurately without arbitrary truncation. Singular points present in the flow field around bluff objects can be treated easily, leading to highly accurate solution with very few degrees of freedom, and without any assumptions being made about the form of the singularity. Bodies of arbitrary shape can be modelled in the normal finite element manner, but only the surface need be discretized. The method can be used with a substructuring technique, permitting the interaction between a number of obstacles to be determined.

In contrast to the boundary element and finite difference methods, the superconvergent patch recovery technique [12] can be used to obtain an improved velocity field [7], and if desired the Zienkiewicz–Zhu error estimator [13] can be used to approximate the error over the entire unbounded domain. This permits application of simple adaptive techniques [14].

This paper uses the scaled boundary finite-element method to address problems of streamlined and bluff objects perturbing a uniform potential flow field of infinite extent. A weighted residual derivation of the method for solution of the Laplace equation is first presented, and new techniques are developed to permit the method to model uniform flow fields. The classical problems of flow around circular and square cylinders are addressed, and the method is shown to yield excellent results with very few degrees of freedom, and to out-perform the boundary element method. Two practical examples are also presented, one being flow around a streamlined object of complex shape, the other being flow around two interacting bluff objects, and comparisons made with finite difference solutions.

2. THE SCALED BOUNDARY FINITE-ELEMENT METHOD FOR POTENTIAL FLOW

Potential flow in two dimensions is governed by the Laplace equation, which may be expressed as

$$\nabla^2\phi = 0 \tag{1}$$

within a domain Ω. Here ϕ is the scalar potential, which may be related to the flow velocity by

$$\mathbf{v} = -\nabla\phi \tag{2}$$

On the boundary of the domain Ω either the value of the potential or the flow velocity must be specified. Designating the entire boundary by Γ, the potential boundary by Γ_ϕ and the velocity boundary by Γ_v, the boundary conditions may be specified as

$$\phi = \bar{\phi} \text{ on } \Gamma_\phi \tag{3}$$

and

$$\phi_{,n} = -\bar{v}_n \quad \text{on } \Gamma_v \tag{4}$$

where n designates the normal to the boundary, the overbar denotes prescribed values and $\phi_{,n}$ is the partial derivative of potential with respect to n. Postponing discussion of prescribed potential boundary conditions to a later stage and prescribing the velocity over the entire boundary ($\Gamma_v = \Gamma$), Equations (1) and (4) can be expressed in weighted residual form (e.g. Reference [15]) as

$$\int_\Omega \nabla^{\mathrm{T}} w \nabla\phi \, \mathrm{d}\Omega - \int_\Gamma w\bar{v}_n \, \mathrm{d}\Gamma = 0 \tag{5}$$

where w is any weighting function. An approximate solution ϕ_h may satisfy this equation for a limited range of weighting functions. The larger the range, the more accurate will be the approximation.

The scaled boundary finite-element method is restricted to domains that can be defined by the scaling of a single piecewise-smooth curve S relative to a scaling centre (x_0, y_0). (Although this requirement may seem restrictive, many practical problems can be modelled using such domains when suitable substructuring is employed.) The defining curve S is taken to be specified by $x(s) = x_0 + x_s(s)$ and $y(s) = y_0 + y_s(s)$, where $s_0 \leqslant s \leqslant s_1$. The circumferential co-ordinate s measures the distance anticlockwise around the curve, and is a function of θ, where θ is indicated in Figure 1. A further restriction on S is that the derivative $\mathrm{d}s/\mathrm{d}\theta$ must not vanish at any point on the curve. The curve may be closed or open.

A normalized radial ξ co-ordinate is defined to have unit value at the curve S. Each value of ξ consequently defines a scaled version of the curve S. Any point in the two-dimensional plane can be specified by the scaled boundary co-ordinates ξ and s. The mapping between this co-ordinate system and the Cartesian co-ordinate system can be expressed by the scaling equations

$$x = x_0 + \xi x_s(s) \tag{6a}$$

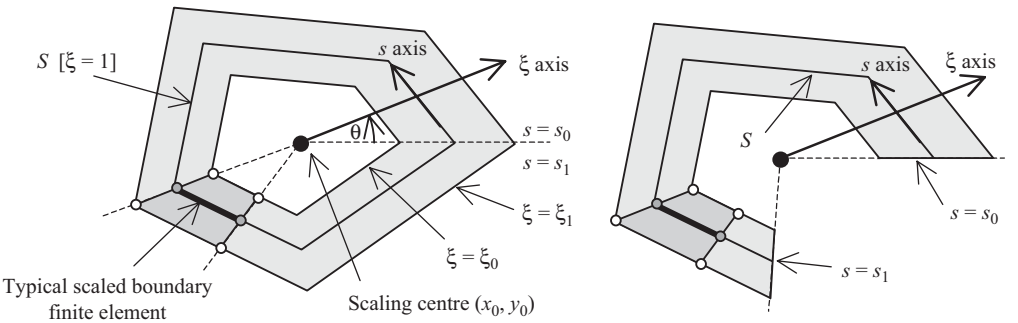

Figure 1. Scaled boundary co-ordinate definition: left, with a closed defining curve; right, with an open defining curve.

$$y = y_0 + \xi y_s(s) \tag{6b}$$

The solution domain Ω is defined as the region defined by $\xi_0 \leqslant \xi \leqslant \xi_1$ and $s_0 \leqslant s \leqslant s_1$. The boundary of this domain Γ is seen to have two sections that are similar to curve S, and two sections that are straight lines radiating from the scaling centre. The two straight sections are termed side-faces. If the curve is closed, the side-faces will coincide.

The scaled boundary finite-element method seeks an approximate solution to Equations (1), (3) and (4) in the form

$$\phi_h(\xi, s) = \mathbf{N}(s)\mathbf{a}(\xi) \tag{7}$$

This represents a discretization of the curve S only by shape functions $\mathbf{N}(s)$. These shape functions can be defined locally over line elements in the conventional finite element manner, with the specification of n nodes on the curve. The n nodal functions represented by the vector $\mathbf{a}(\xi)$ are analogous to nodal values in the standard finite element method. At each node i the function $a_i(\xi)$ represents the variation of potential in the radial direction. At any value of ξ the shape functions interpolate between the nodal potential values in the circumferential direction. A typical scaled boundary finite element is illustrated in Figure 1, together with the region of the domain modelled by this element.

Unbounded domains can be treated conveniently by taking $\xi_0 = 1$ and $\xi_1 = \infty$. Bounded domains containing the scaling centre are modelled by taking $\xi_0 = 0$ and $\xi_1 = 1$. In such cases the defining curve S becomes the discretized portion of the boundary. (The side-faces are not discretized.)

Using conventional techniques the operator ∇ can be mapped to the scaled boundary co-ordinate system (see Appendix A) by

$$\nabla = \mathbf{b}_1(s)\frac{\partial}{\partial \xi} + \frac{1}{\xi}\mathbf{b}_2(s)\frac{\partial}{\partial s} \tag{8}$$

where $\mathbf{b}_1(s)$ and $\mathbf{b}_2(s)$ are dependent only on the definition of S. Substituting Equations (7) and (8) into Equation (2), the approximate velocities can be expressed in terms of the scaled

boundary co-ordinates as

$$\mathbf{v}_h(\xi,s) = -\mathbf{B}_1(s)\mathbf{a}(\xi),_\xi - \frac{1}{\xi}\mathbf{B}_2(s)\mathbf{a}(\xi) \tag{9}$$

where, for convenience,

$$\mathbf{B}_1(s) = \mathbf{b}_1(s)\mathbf{N}(s) \tag{10}$$

$$\mathbf{B}_2(s) = \mathbf{b}_2(s)\mathbf{N}(s),_s \tag{11}$$

Using the Galerkin approach, the weighting function w can be formulated using the same shape functions along S as the approximation for the potential (Equation (7)).

$$w(\xi,s) = \mathbf{N}(s)\mathbf{w}(\xi) = \mathbf{w}(\xi)^{\mathrm{T}}\mathbf{N}(s)^{\mathrm{T}} \tag{12}$$

This restricts the form of the weighting function in the circumferential direction, but not in the radial direction. Substituting Equations (7) and (12) into Equation (5), the weighted residual statement becomes

$$\int_\Omega [\nabla\mathbf{N}(s)\mathbf{w}(\xi)]^{\mathrm{T}}[\nabla\mathbf{N}(s)\mathbf{a}(\xi)]\,\mathrm{d}\Omega - \int_\Gamma \mathbf{w}(\xi)^{\mathrm{T}}\mathbf{N}(s)^{\mathrm{T}}\bar{v}_n\,\mathrm{d}\Gamma = 0 \tag{13}$$

With the addition of Equations (8), (10) and (11), Equation (13) becomes

$$\int_\Omega \left[\mathbf{B}_1(s)\mathbf{w}(\xi),_\xi + \frac{1}{\xi}\mathbf{B}_2(s)\mathbf{w}(\xi)\right]^{\mathrm{T}} \left[\mathbf{B}_1(s)\mathbf{a}(\xi),_\xi + \frac{1}{\xi}\mathbf{B}_2(s)\mathbf{a}(\xi)\right] \mathrm{d}\Omega - \int_\Gamma \mathbf{w}(\xi)^{\mathrm{T}}\mathbf{N}(s)^{\mathrm{T}}\bar{v}_n\,\mathrm{d}\Gamma = 0 \tag{14}$$

Expanding and integrating the domain integrals containing $\mathbf{w}(\xi),_\xi$ with respect to ξ using Green's theorem, and noting that $\mathrm{d}\Omega = |J|\xi\,\mathrm{d}\xi\,\mathrm{d}s$ (Equation (A6)), yields

$$\begin{aligned}
&\int_S \mathbf{w}(\xi_1)^{\mathrm{T}}\mathbf{B}_1(s)^{\mathrm{T}}\mathbf{B}_1(s)\xi_1\mathbf{a}(\xi_1),_\xi |J|\,\mathrm{d}s - \int_S \mathbf{w}(\xi_0)^{\mathrm{T}}\mathbf{B}_1(s)^{\mathrm{T}}\mathbf{B}_1(s)\xi_0\mathbf{a}(\xi_0),_\xi |J|\,\mathrm{d}s \\
&\quad - \int_{\xi_0}^{\xi_1}\int_S \mathbf{w}(\xi)^{\mathrm{T}}\mathbf{B}_1(s)^{\mathrm{T}}\mathbf{B}_1(s)\{\mathbf{a}(\xi),_\xi + \xi\mathbf{a}(\xi),_{\xi\xi}\}|J|\,\mathrm{d}s\,\mathrm{d}\xi \\
&\quad + \int_S \mathbf{w}(\xi_1)^{\mathrm{T}}\mathbf{B}_1(s)^{\mathrm{T}}\mathbf{B}_2(s)\mathbf{a}(\xi_1),_\xi |J|\,\mathrm{d}s - \int_S \mathbf{w}(\xi_0)^{\mathrm{T}}\mathbf{B}_1(s)^{\mathrm{T}}\mathbf{B}_2(s)\mathbf{a}(\xi_0),_\xi |J|\,\mathrm{d}s \\
&\quad - \int_{\xi_0}^{\xi_1}\int_S \mathbf{w}(\xi)^{\mathrm{T}}\mathbf{B}_1(s)^{\mathrm{T}}\mathbf{B}_2(s)\mathbf{a}(\xi),_\xi |J|\,\mathrm{d}s\,\mathrm{d}\xi \\
&\quad + \int_{\xi_0}^{\xi_1}\int_S \mathbf{w}(\xi)^{\mathrm{T}}\mathbf{B}_2(s)^{\mathrm{T}}\mathbf{B}_1(s)\mathbf{a}(\xi),_\xi |J|\,\mathrm{d}s\,\mathrm{d}\xi + \int_{\xi_0}^{\xi_1}\int_S \mathbf{w}(\xi)^{\mathrm{T}}\mathbf{B}_2(s)^{\mathrm{T}}\mathbf{B}_2(s)\frac{1}{\xi}\mathbf{a}(\xi)|J|\,\mathrm{d}s\,\mathrm{d}\xi
\end{aligned}$$

$$- \int_S \mathbf{w}(\xi_1)^{\mathrm{T}} \mathbf{N}(s)^{\mathrm{T}} \bar{v}_n(\xi_1, s) \xi_1 \, \mathrm{d}s - \int_{\xi_0}^{\xi_1} \mathbf{w}(\xi)^{\mathrm{T}} \mathbf{N}(s_0)^{\mathrm{T}} \bar{v}_n(\xi, s_0) |J| \, \mathrm{d}\xi$$

$$+ \int_S \mathbf{w}(\xi_0)^{\mathrm{T}} \mathbf{N}(s)^{\mathrm{T}} (-\bar{v}_n(\xi_0, s)) \xi_0 \, \mathrm{d}s + \int_{\xi_0}^{\xi_1} \mathbf{w}(\xi)^{\mathrm{T}} \mathbf{N}(s_1)^{\mathrm{T}} (-\bar{v}_n(\xi, s_1)) |J| \, \mathrm{d}\xi = 0 \tag{15}$$

Note that during integration of the normal flows along the boundary, reversal of the direction of the integration results in reversal of the sign of the normal velocity in the last two terms. The following coefficient matrices are now introduced for convenience.

$$\mathbf{E}_0 = \int_S \mathbf{B}_1(s)^{\mathrm{T}} \mathbf{B}_1(s) |J| \, \mathrm{d}s \tag{16a}$$

$$\mathbf{E}_1 = \int_S \mathbf{B}_2(s)^{\mathrm{T}} \mathbf{B}_1(s) |J| \, \mathrm{d}s \tag{16b}$$

$$\mathbf{E}_2 = \int_S \mathbf{B}_2(s)^{\mathrm{T}} \mathbf{B}_2(s) |J| \, \mathrm{d}s \tag{16c}$$

$$\mathbf{F}_s(\xi) = \mathbf{N}(s_0)^{\mathrm{T}} (-\bar{v}_n(\xi, s_0)) |J(s_0)| + \mathbf{N}(s_1)^{\mathrm{T}} (-\bar{v}_n(\xi, s_1)) |J(s_1)| \tag{16d}$$

Simplifying Equation (15) by introducing these coefficient matrices and collecting common terms

$$\mathbf{w}(\xi_1)^{\mathrm{T}} \left[\mathbf{E}_0 \xi_1 \mathbf{a}(\xi_1)_{,\xi} + \mathbf{E}_1^{\mathrm{T}} \mathbf{a}(\xi_1) + \int_S \mathbf{N}(s)^{\mathrm{T}} (-\bar{v}_n(\xi_1, s)) \xi_1 \, \mathrm{d}s \right]$$

$$- \mathbf{w}(\xi_0)^{\mathrm{T}} \left[\mathbf{E}_0 \xi_0 \mathbf{a}(\xi_0)_{,\xi} + \mathbf{E}_1^{\mathrm{T}} \mathbf{a}(\xi_0) - \int_S \mathbf{N}(s)^{\mathrm{T}} (-\bar{v}_n(\xi_0, s)) \xi_0 \, \mathrm{d}s \right]$$

$$- \int_{\xi_0}^{\xi_1} \mathbf{w}(\xi)^{\mathrm{T}} \left\{ \mathbf{E}_0 \xi \mathbf{a}(\xi)_{,\xi\xi} + [\mathbf{E}_0 + \mathbf{E}_1^{\mathrm{T}} - \mathbf{E}_1] \mathbf{a}(\xi)_{,\xi} - \mathbf{E}_2 \frac{1}{\xi} \mathbf{a}(\xi) - \mathbf{F}_s(\xi) \right\} \mathrm{d}\xi = 0 \tag{17}$$

This equation will be satisfied for any set of weighting functions $\mathbf{w}(\xi)$ providing the following conditions are met.

$$\int_S \mathbf{N}(s)^{\mathrm{T}} (-\bar{v}_n(\xi_0, s)) \xi_0 \, \mathrm{d}s = \mathbf{E}_0 \xi_0 \mathbf{a}(\xi_0)_{,\xi} + \mathbf{E}_1^{\mathrm{T}} \mathbf{a}(\xi_0) \tag{18}$$

$$\int_S \mathbf{N}(s)^{\mathrm{T}} (-\bar{v}_n(\xi_1, s)) \xi_1 \, \mathrm{d}s = -\mathbf{E}_0 \xi_1 \mathbf{a}(\xi_1)_{,\xi} - \mathbf{E}_1^{\mathrm{T}} \mathbf{a}(\xi_1) \tag{19}$$

$$\mathbf{E}_0 \xi^2 \mathbf{a}(\xi)_{,\xi\xi} + [\mathbf{E}_0 + \mathbf{E}_1^{\mathrm{T}} - \mathbf{E}_1] \xi \mathbf{a}(\xi)_{,\xi} - \mathbf{E}_2 \mathbf{a}(\xi) = \xi \mathbf{F}_s(\xi) \tag{20}$$

Equation (20) is termed the scaled boundary finite-element equation. Effectively the Laplace equation has been weakened in the circumferential direction in a finite element manner, but

remains strong in the radial direction. Equation (18) indicates a discretization of the inner portion of the boundary, which is a scaled version of the discretization of S, and relates the integrated nodal flows into the domain across this part of the boundary to the potential field at the same nodes. In a similar manner, Equation (19) indicates a scaled discretization of the outer portion of the boundary, and relates integrated nodal flows into the domain across this portion of the boundary to the boundary potential field.

Since the side-faces are not discretized, the variation of normal velocity remains analytical, as indicated by Equation (16d). If curve S is closed, the side-faces coincide, and the flow across the side-faces is equal and opposite, so the term $\mathbf{F}_s(\xi)$ vanishes. This term also vanishes if the side-faces are impermeable.

3. SOLUTION PROCESS

To permit domains modelled by the scaled boundary finite-element method to be used either alone or as substructures, the relationship between the potential and the integrated nodal flows over the discretized portion of the boundary will be obtained in the standard discrete form

$$\mathbf{Ha} = \mathbf{f} \tag{21}$$

where $\mathbf{a}$ is a vector containing the potential values at the boundary nodes, $\mathbf{f}$ contains the integrated flows into the domain at the boundary nodes and $\mathbf{H}$ is an square matrix. Once $\mathbf{H}$ has been constructed, boundary conditions can be applied to suitable subsets of $\mathbf{a}$ and $\mathbf{f}$, and the system of equations solved.

The construction of $\mathbf{H}$ will now be described. Equation (20) is considered initially in homogenous form, corresponding to a closed defining curve S or impermeable side-faces. By inspection, solutions to this differential equation take the form

$$\mathbf{a}(\xi) = c_1 \xi^{-\lambda_1} \mathbf{a}_1 + c_2 \xi^{-\lambda_2} \mathbf{a}_2 + \cdots \tag{22}$$

where the exponents $-\lambda_i$ and corresponding vectors $\mathbf{a}_i$ may be interpreted as independent potential fields which closely satisfy the Laplace equation in the ξ direction. The constants c_i represent the contribution of each potential 'mode' to the solution, and are dependent on the boundary conditions.

Each potential mode takes the form

$$\mathbf{a}_i(\xi) = \xi^{-\lambda_i} \mathbf{a}_i \tag{23}$$

The vector $\mathbf{a}_i$ can be identified as the modal potentials at the nodes on the curve S, while λ_i can be identified as a modal scaling factor for the radial direction. Substituting this solution into Equation (20) with $\mathbf{F}_s(\xi) = 0$ yields the quadratic eigenproblem

$$[\lambda_i^2 \mathbf{E}_0 - \lambda_i [\mathbf{E}_1^{\mathrm{T}} - \mathbf{E}_1] - \mathbf{E}_2] \mathbf{a}_i = 0 \tag{24}$$

This eigenproblem can be solved using standard techniques, yielding $2n$ potential modes, where n is the number of nodes used to discretize S, and hence is also the size of the coefficient matrices.

Bounded problems can be represented conveniently by taking $\xi_0 = 0$ and $\xi_1 = 1$. For such problems only modes with finite potential at the scaling centre will have non-zero integration

constants. The modes for which the real parts of the eigenvalues are negative will satisfy this requirement and will automatically satisfy Equation (18). The potential values at the boundary nodes for each mode will be $\mathbf{a}_i$.

Similarly, unbounded domains can be represented by taking $\xi_0 = 1$ and $\xi_1 = \infty$. Unbounded domains generally require that the potential remains finite at infinity. Modes with eigenvalues with positive real parts will satisfy this requirement, and will automatically satisfy Equation (19). The potential values at the boundary nodes for each mode will also be $\mathbf{a}_i$.

One constant potential mode with unit values at all boundary nodes and an eigenvalue of zero is also be admissible in both bounded and unbounded cases. Solution of the single eigenproblem is found to yield n potential modes that are admissible for a bounded domain containing the scaling centre, and n modes that are admissible for the unbounded domain represented by the same defining curve. The subset of n flow modes admissible for the type of problem under consideration are used to form the columns of an n by n matrix $\mathbf{A}$.

For any given set of boundary node potentials $\mathbf{a}$ the integration constants for the modes may be determined as

$$\mathbf{c} = \mathbf{A}^{-1}\mathbf{a} \tag{25}$$

where $\mathbf{c}$ is a vector containing n of integration constants.

The flows into the domain required at the boundary nodes by each potential mode are obtained for the bounded case by substituting Equation (23) into Equation (19) (which is evaluated at $\xi_1 = 1$) as

$$\mathbf{q}_i = -[\mathbf{E}_1^{\mathrm{T}} - \lambda\mathbf{E}_0]\mathbf{a}_i \tag{26}$$

or for the unbounded case by substituting Equation (23) into Equation (18) (which is evaluated at $\xi_0 = 1$) as

$$\mathbf{q}_i = [\mathbf{E}_1^{\mathrm{T}} - \lambda\mathbf{E}_0]\mathbf{a}_i \tag{27}$$

Placing the integrated normal flows into the domain corresponding to the potential modes in the columns of $\mathbf{A}$ in the columns of another n by n matrix $\mathbf{Q}$, the total integrated normal flows into the domain at the discretized boundary corresponding to a set of boundary node potentials $\mathbf{a}$ are

$$\mathbf{f} = \mathbf{Q}\mathbf{c} = \mathbf{Q}\mathbf{A}^{-1}\mathbf{a} \tag{28}$$

and hence

$$\mathbf{H} = \mathbf{Q}\mathbf{A}^{-1} \tag{29}$$

Equation (21) can then be solved for all boundary potentials which are not prescribed, after which Equation (25) can be used to determine the integration constants. With the integration constants known the entire potential field can be found by substituting Equation (22) into Equation (7), and the velocity field by substituting Equation (22) into Equation (9).

In summary the solution process consists of: (i) construction of the coefficient matrices (Equation (16)), which can be done element by element over S in the usual finite element manner; (ii) solution of the quadratic eigenproblem (Equation (24)), extraction of the set of n eigenvalues and vectors appropriate to the type of domain under consideration, and

computation of the corresponding integrated normal flows into the domain (Equations (26) and (27)); (iii) construction of the **H** matrix for the domain (Equation (29)); (iv) solution of Equation (21) for those boundary potentials and integrated flows into the domain which are not prescribed; (v) determination of the integration constants (Equation (25)); and (vi) computation of the potential and velocity fields (Equation (22) with Equations (7) and (9)).

As in the standard finite element method, the velocity field obtained by Equation (9) is raw and generally discontinuous in the circumferential direction between elements. A better approximation can be obtained by applying the superconvergent patch recovery technique [12]. The extension of this technique to the scaled boundary finite-element method involves the recovery of velocity fields for each mode. This extension is covered in detail in Reference [7]. The availability of an accurate recovered stress field allows the widely used Zienkiewicz–Zhu error estimator [13] to be applied to the method. This in turn allows adaptive techniques to be applied [14].

4. BOUNDARY CONDITIONS

4.1. Discretized boundary and infinity

The class of problem under consideration here is that of flow around shapes placed in a uniform potential flow field of infinite extent. Assuming that the uniform flow occurs in the global x-direction and has magnitude V, the appropriate boundary conditions are

$$\nabla\phi = \begin{Bmatrix} -V \\ 0 \end{Bmatrix} \quad \text{at } \xi = \infty \tag{30}$$

and

$$\phi_{,n} = 0 \quad \text{at } \xi = 1 \tag{31}$$

The first boundary condition implies infinite positive potential at $x = -\infty$ and infinite negative potential at $x = +\infty$. Since the potential modes in the scaled boundary finite-element method are restricted to those with finite potential at infinity (and consequently no normal flow at infinity), an additional particular solution to the Laplace equation must be included to permit this boundary condition to be satisfied. This solution is obtained by ignoring the second boundary condition. (The second boundary condition will be satisfied by combination of this particular solution with the approximate general solution obtained by the scaled boundary finite-element method.)

Arbitrarily setting the potential at $x = 0$ to zero, a particular solution for the potential field satisfying Equation (30) is

$$\phi_v = -Vx \tag{32}$$

The subscript v is adopted to indicate this particular solution. Mapping to the scaled boundary co-ordinate system

$$\phi_v = -V(x_0 + \xi x_s(s)) \tag{33}$$

The derivative of this potential field with respect to the normal at the boundary of the obstacle is

$$\phi_{v,n} = -Vn_x(s) \tag{34}$$

where $n_x(s)$ is the x component of the unit vector normal to the surface at s. The integrated nodal flows into the domain across the discretized boundary due to the particular solution are therefore

$$\mathbf{q}_v = \int_{\Gamma_d} \mathbf{N}(s)^{\mathrm{T}}(-Vn_x(s))\,\mathrm{d}\Gamma \tag{35}$$

where Γ_d represents the discretized portion of the boundary. For the total integrated flows across the boundary to be zero (the second boundary condition)

$$\mathbf{Ha} + \mathbf{q}_v = \mathbf{0} \tag{36}$$

Solution of this equation yields nodal potential values as before, but now the particular solution must be included in the final potential field.

$$\phi_h(\xi, s) = \mathbf{N}(s)\mathbf{a}(\xi) - V(x_0 + \xi x_s(s)) \tag{37}$$

The final velocity field then becomes

$$\mathbf{v}_h(\xi, s) = -\mathbf{B}_1(s)\mathbf{a}(\xi)_{,\xi} - \frac{1}{\xi}\mathbf{B}_2(s)\mathbf{a}(\xi) + \begin{Bmatrix} V \\ 0 \end{Bmatrix} \tag{38}$$

4.2. Side-faces

Should the defining curve of the domain be open, and the boundary conditions on the side-faces not be defined in terms of potential, for the velocity component normal to the side-faces in the final velocity field to be zero

$$\bar{v}_n(\xi, s_0) + Vn_x(\xi, s_0) = 0 \tag{39}$$

and

$$\bar{v}_n(\xi, s_1) + Vn_x(\xi, s_1) = 0 \tag{40}$$

Since the side-faces are straight lines, the x component of the unit normal is constant for each, and so

$$\mathbf{F}_s(\xi) = \mathbf{N}(s_0)^{\mathrm{T}} Vn_x(s_0)|J(s_0)| + \mathbf{N}(s_1)^{\mathrm{T}} Vn_x(s_1)|J(s_1)| = \mathbf{F}_s \tag{41}$$

Inspection of the non-homogenous Equation (20) indicates the particular solution is of the form

$$\mathbf{a}_s(\xi) = \xi \mathbf{a}_s \tag{42}$$

Substitution of this particular solution into Equation (20) allows the potentials at the boundary node points to be found as

$$\mathbf{a}_s = [\mathbf{E}_0 - \mathbf{E}_1^{\mathrm{T}} + \mathbf{E}_1 - \mathbf{E}_2]^{-1}\mathbf{F}_s \tag{43}$$

The nodal flows into the domain generated at the discretized section of the boundary by this particular solution are obtained by substitution of Equation (42) into Equation (26) or (27), according to the type of domain. These flows are denoted $\mathbf{q}_s$. The integration constants for the general solution of the homogenous equation must now be determined to preserve boundary conditions at the discretized boundary. Since the complete solution to the scaled boundary finite-element equation is now

$$\mathbf{a}(\xi) = \xi \mathbf{a}_s + c_1 \xi^{-\lambda_1} \mathbf{a}_1 + c_2 \xi^{-\lambda_2} \mathbf{a}_2 + \cdots \tag{44}$$

the potentials at the nodes on the discretized boundary (at $\xi = 1$) are now related to the integration constants by

$$\mathbf{c} = \mathbf{A}^{-1}\{\mathbf{a} - \mathbf{a}_s\} \tag{45}$$

while the boundary conditions will be satisfied when

$$\mathbf{Q}\mathbf{c} + \mathbf{q}_v + \mathbf{q}_s = 0 \tag{46}$$

leading to

$$\mathbf{H}\{\mathbf{a} - \mathbf{a}_s\} + \mathbf{q}_v + \mathbf{q}_s = \mathbf{0} \tag{47}$$

Application of appropriate boundary conditions to $\mathbf{a}$ allows solution of all nodal potentials, after which the integration constants can be determined using Equation (45). Substitution of Equation (44) into Equations (37) and (38) then provides the entire potential and velocity fields.

5. EXAMPLES

5.1. Flow around a circular cylinder

The accuracy of the method is first demonstrated using the classical example of flow around a circular cylinder. The exact solution of this problem is well known. If the potential at $x = 0$ is taken as zero, the free stream velocity is V, and the radius of the cylinder is R the potential field in standard polar co-ordinates is

$$\phi = -V\left(1 + \frac{R^2}{r^2}\right) r \cos\theta \tag{48}$$

The variation of the tangential velocity around the cylinder follows as

$$v_t = 2V \sin\theta \tag{49}$$

One quarter of the problem is modelled using a single unbounded domain, as illustrated in Figure 2. The normal flow on the first side-face is prescribed as zero, as is the potential on the second side-face, enforcing the symmetry condition. The boundary of the cylinder is discretized with three-noded quadratic elements. Three meshes are used to illustrate the convergence of the method. The coarse mesh consists of two elements. The other two meshes (referred to as intermediate and fine) are constructed by binary subdivision of the coarse mesh, and consist of four and eight elements respectively. These meshes are illustrated in Figure 3.

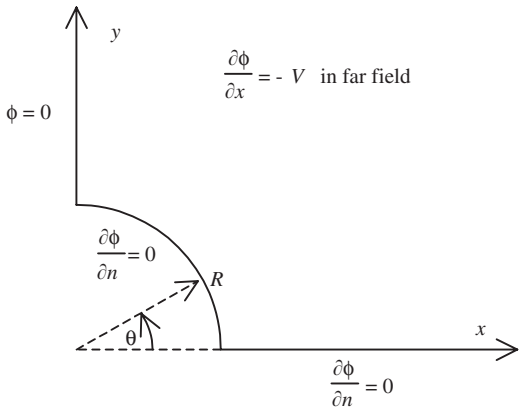

Figure 2. Example 1, a circular cylinder in a uniform flow.

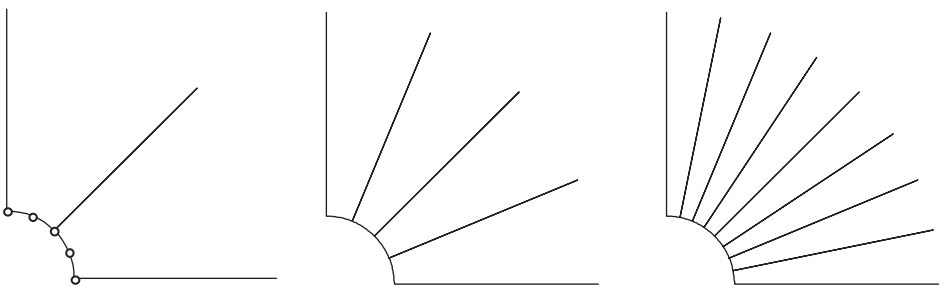

Figure 3. Coarse, intermediate and fine unbounded scaled boundary finite-element meshes for Example 1.

Figure 4 plots the variation of potential around the cylinder computed with the different meshes, along with the exact solution. All meshes provide excellent agreement with the exact solution. Figure 5 plots the variation of the tangential velocity around the cylinder. The velocity is recovered using the superconvergent patch recovery technique [12]. The results obtained using the intermediate and fine meshes are indistinguishable from the exact solution. The velocity computed by the coarsest mesh shows some small error, but since only one patch can be formed in the recovery process (and so the other nodal values must be extrapolated), the results are still impressive.

This example has also been analysed by Lesnic *et al.* [10] using a boundary element method and modelling the complete cylinder with meshes of 20, 40 and 80 elements. The relative accuracy of comparable scaled boundary finite-element solutions is determined by modelling the quarter cylinder with meshes of 5, 10 and 20 elements. Table I lists the computed dimensionless velocities in the x-direction computed at 5 points along the x-axis with the scaled boundary finite-element method (SBFEM), the velocities computed by Lesnic *et al.* [10] using quadratic boundary elements (QBEM), and the analytical solution. At the identical levels of discretization, the scaled boundary finite-element results are more accurate,

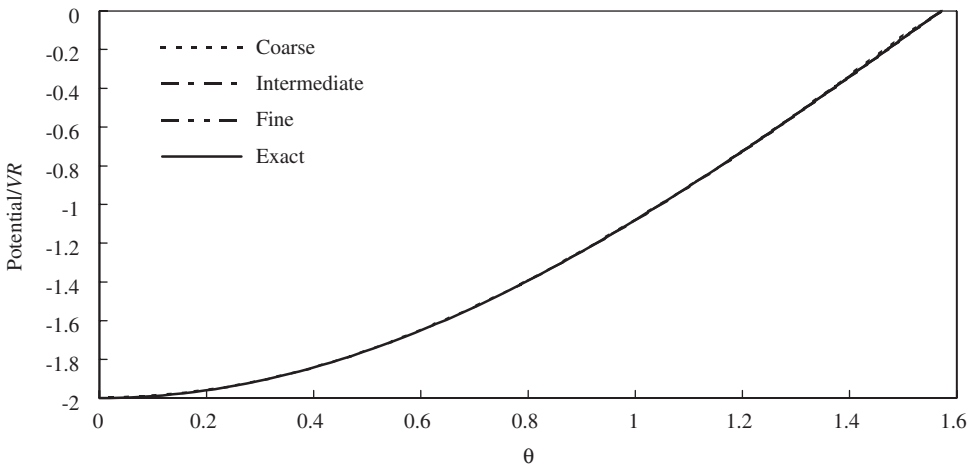

Figure 4. Variation of potential around circular cylinder (Example 1).

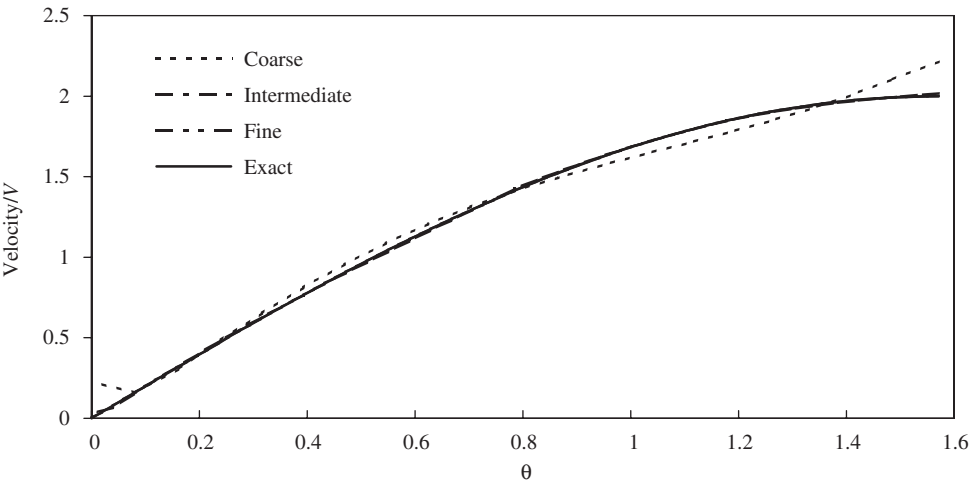

Figure 5. Variation of tangential velocity around circular cylinder (Example 1).

and generally the convergence is uniform. With 20 elements on the quarter circle the error in velocity at each point is less than 0.1%.

Similar accuracy is present at the cylinder surface. The dimensionless velocities computed at four points around the quarter cylinder are presented in Table II. Once again, with identical levels of boundary discretization the scaled boundary finite-element method is more accurate, and convergence with increasing mesh density is uniform.

Table I. Variation in dimensionless velocity in x-direction computed for Example 1 with meshes of increasing density.

x/R	SBFEM	QBEM	Analytical
1.1	0.1671	0.1873	0.1736
	0.1731	0.1742	
	0.1735	0.1675	
1.3	0.4037	0.4054	0.4083
	0.4080	0.4056	
	0.4083	0.4053	
1.5	0.5521	0.5557	0.5556
	0.5553	0.5552	
	0.5555	0.5548	
1.7	0.6513	0.6592	0.6540
	0.6538	0.6548	
	0.6540	0.6542	
1.9	0.7208	0.7260	0.7230
	0.7229	0.7243	
	0.7230	0.7236	

Table II. Variation in dimensionless velocities computed on the surface of the cylinder of Example 1 with meshes of increasing density.

	SBFEM		QBEM		Analytical	
θ (degrees)	v_x	v_y	v_x	v_y	v_x	v_y
0	−0.0078	0.0138	0.0400	−0.0080	0.0000	0.0000
	−0.0005	0.0019	0.0100	0.0030		
	0.0000	0.0002	0.0090	0.0080		
22.5	0.2951	−0.7073	0.2637	−0.7224	0.2928	−0.7071
	0.2930	−0.7070	0.2795	−0.7192		
	0.2929	−0.7071	0.2826	−0.7182		
45	1.0000	−0.9984	1.0290	−1.0290	1.0000	−1.0000
	1.0000	−1.0000	1.0160	−1.0160		
	1.0000	−1.0000	1.0122	−1.0122		
67.5	1.7049	−0.7073	1.7427	−0.7273	1.7071	−0.7071
	1.7070	−0.7070	1.7297	−0.7213		
	1.7071	−0.7071	1.7134	−0.7198		
90	2.0078	0.0143	2.0350	0.0000	2.0000	0.0000
	2.0005	0.0020	2.0185	0.0000		
	2.0000	0.0003	2.0116	0.0000		

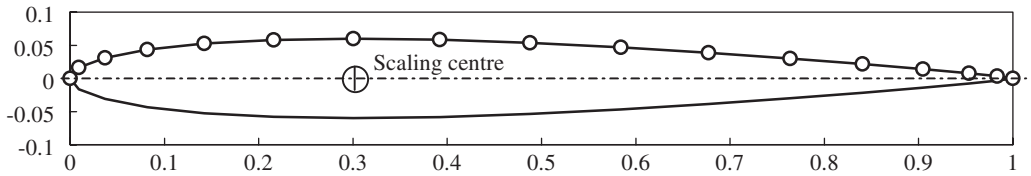

Figure 6. NACA 0012 wing section, showing node positions used in the coarse model (Example 2).

5.2. *Flow around a wing section*

The geometry of Example 1 is very simple, and the exact solution is very smooth. The second example examines the practical problem of flow around a wing section. The symmetric NACA 0012 wing section is chosen, as the definition of this section is freely available [16]. The section is oriented so the axis of symmetry is aligned with the x-axis, allowing the Kutta–Joukowski condition at the trailing edge to be satisfied automatically.

Tangential velocity varies sharply around the leading and trailing edges of the section. The low aspect ratio severely tests the scaled boundary finite-element method, since some of the circumferential elements near the trailing edge are almost parallel to lines radiating from the scaling centre.

Advantage is taken of the symmetry of the problem, and half of the domain is modelled. The boundary conditions discussed in the first example are applied. However, since there is no vertical axis of symmetry along which the potential is prescribed, and since the potential field can only be found to within a constant, the potential at the leading edge is defined arbitrarily as zero to allow a solution to be obtained. Three meshes of increasing fineness are used. The coarse mesh consists of eight three-noded quadratic elements. The locations of the nodes for this model are indicated in Figure 6, which also plots the lower portion of the section for clarity. Similar intermediate and fine meshes, with 17 and 33 elements, respectively, are also used. The scaling centre for all models is chosen to be a distance of 30% of the total section length behind the leading edge.

Since the potential converges rapidly, only the velocity tangential to the surface is presented in Figure 7. Although convergence of the velocity is not as rapid as in Example 1, the velocities computed by the intermediate mesh are in close agreement with the fine mesh. The velocity error observed near the leading edge in the coarse mesh solution may be attributed to the action of the velocity recovery algorithm in an edge region of high velocity variation. Once the mesh is refined, convergence is soon obtained. An independent solution obtained using finite difference analysis is provided in Figure 7 to indicate the accuracy of the results. This example demonstrates that even for obstacles with low aspect ratio, accurate solutions can be obtained using the scaled boundary finite-element method.

5.3. *Flow around a square cylinder*

The analytical solution for the first example is smooth in both the primary quantity (the potential) and the derived quantity (the velocity). The third example is a square cylinder in a uniform flow. In this case the correct solution contains singularities in the velocity field at the corners. The symmetry of the problem allows one quarter of the domain to be modelled.

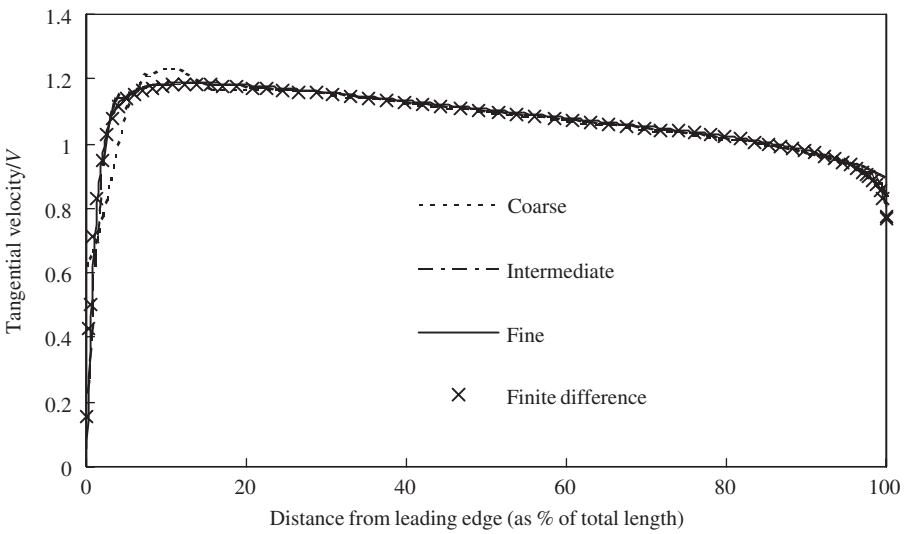

Figure 7. Tangential velocity computed over the NACA 0012 wing section (Example 2).

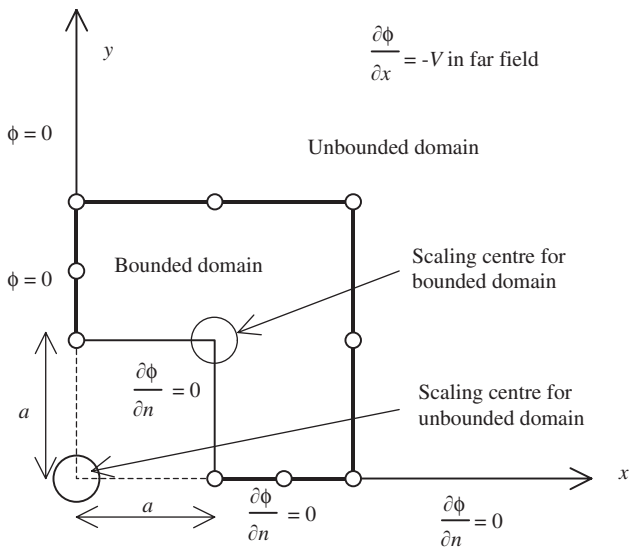

Figure 8. Substructured model for Example 3, flow around a square cylinder.

A key feature of the scaled boundary finite-element method is its ability to accurately model singularities at the scaling centre. For this reason, the cylinder corner is taken as a scaling centre. However, a domain containing the scaling centre must be bounded, so this example requires the solution domain to be substructured into a bounded domain and an unbounded domain, as indicated in Figure 8. The scaling centre for the unbounded domain is taken as the origin, while the scaling centre for the bounded domain is taken as the corner of the cylinder.

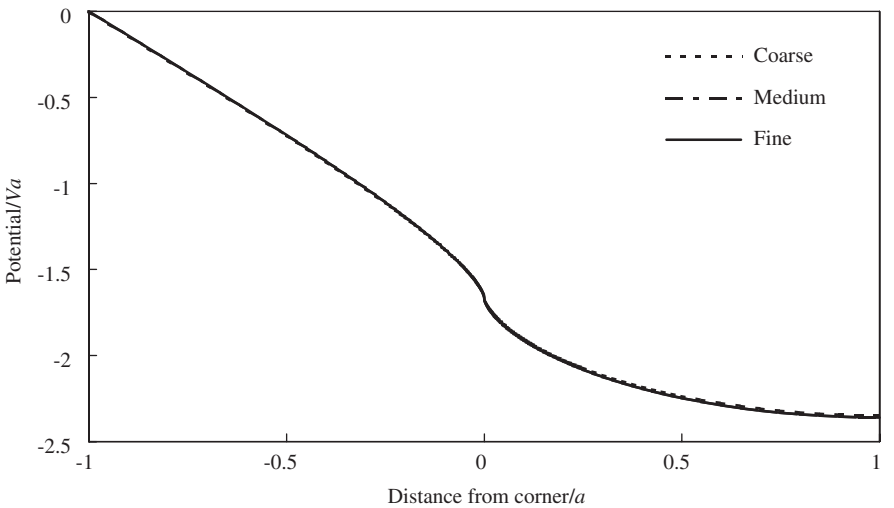

Figure 9. Computed variation of potential along the surface of the square cylinder.

Three-noded line elements are used to discretize each scaled boundary domain. The coarse mesh is indicated in Figure 8. Two elements are used to discretize the unbounded domain, and four elements are used to discretize the bounded domain. Intermediate and fine meshes are constructed from this model by binary subdivision.

The variation in potential computed over the surface of the square cylinder is presented in Figure 9. Even the coarsest mesh provides excellent results. The potential is discontinuous at the corner, and this discontinuity is reproduced accurately. The variation in tangential velocity around the corner is shown in Figure 10. Again, even the coarsest mesh provides an excellent approximation, and the computed velocity contains a true singularity at the corner. In contrast, even after removing the singularity (and employing a similar subdivision into bounded and unbounded domains) the boundary element approach of Lesnic *et al.* [11] requires 90 elements over the quarter cylinder to achieve accurate results. Two finite difference solutions are also plotted in Figure 10. The coarse grid (80×80) leads to a poor approximation of the velocity variation in the vicinity of the corner, while the results of the fine grid (320×320) show good agreement with the scaled boundary finite-element results, except very near the corner. The slow rate of convergence of the finite difference method is in stark contrast to that of the scaled boundary finite-element method.

The excellent results obtained in this example, even for the very coarse mesh, may be attributed to the use of side-faces to model the boundaries of the obstacle. The solution obtained by the scaled boundary finite-element method is analytical along these side-faces. In the first two examples the boundaries of the obstacle were discretized. This example demonstrates the level of accuracy that can be achieved by taking advantage of the key features of the scaled boundary finite-element method.

5.4. Flow around two square cylinders

The fourth example computes the flow around two square cylinders in close proximity. This illustrates how substructuring allows the technique to solve interaction problems. The horizontal

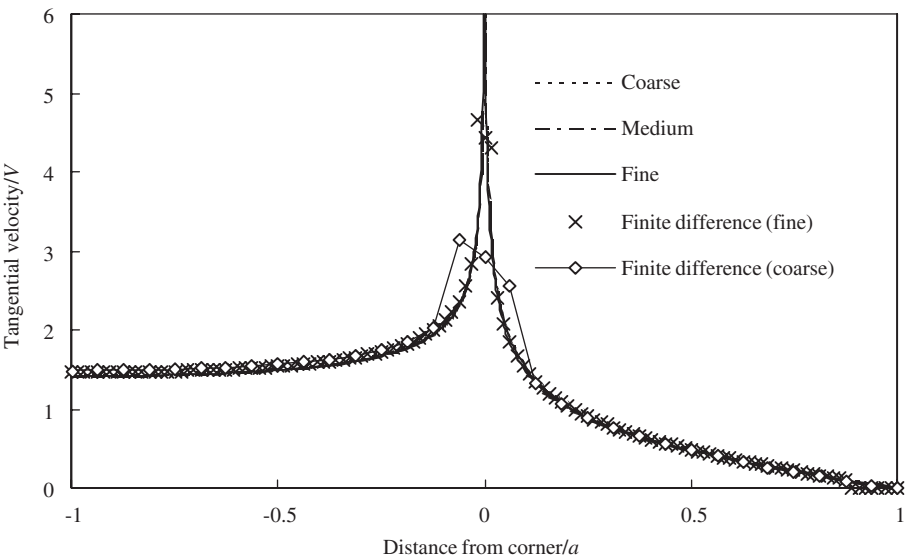

Figure 10. Computed variation of tangential velocity along the surface of the square cylinder of Example 2.

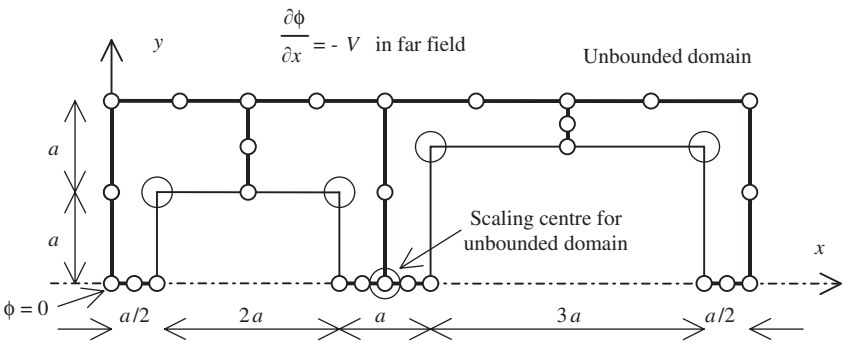

Figure 11. Model for the two square cylinders of Example 4, consisting of four bounded subdomains and one unbounded subdomain.

axes of symmetry of the cylinders are taken to coincide, and one half of the symmetric problem modelled. The trailing cylinder is 50% larger than the leading cylinder. The model consists of four bounded subdomains and one unbounded subdomain, as illustrated in Figure 11. As the accuracy of a rather coarse mesh is established by Example 3, only a coarse mesh is used to solve this problem. The variation of tangential velocity computed around the two cylinders is plotted in Figure 12. The singularities at the corners are evident, and the interaction between the two cylinders is demonstrated clearly by the reduction in velocity along the side of the leading cylinder. The accuracy of these results is established by comparison with finite difference results obtained using a $0.1a$ grid extending a distance $20a$ from the origin in each direction. These results are also plotted in Figure 11. Excellent agreement is evident,

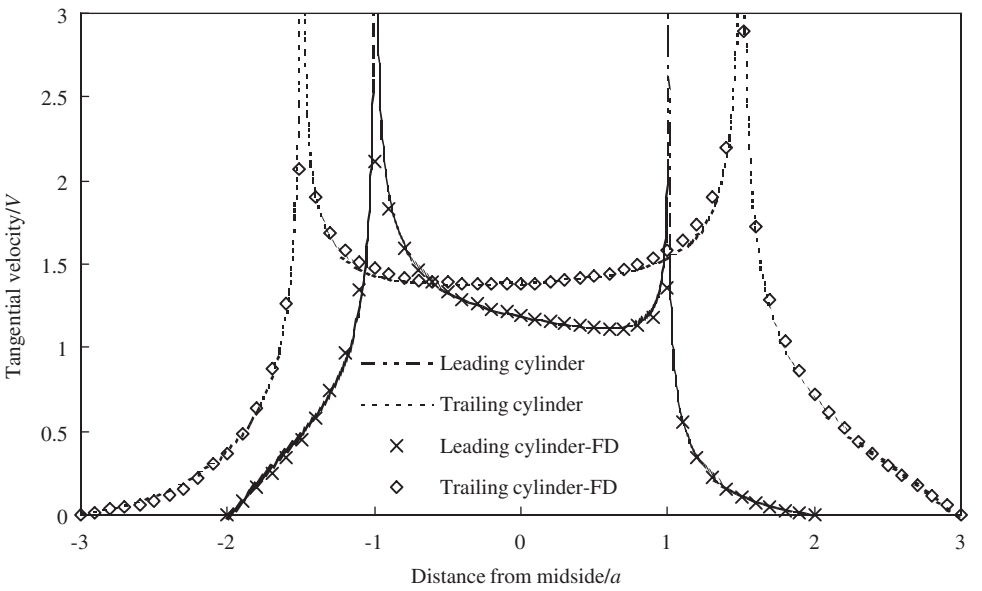

Figure 12. Computed variation of tangential velocity over the square cylinders of Example 4.

except very close to the corners, where the scaled boundary finite-element results are clearly superior.

6. CONCLUSIONS

This paper applies the scaled boundary finite-element method to problems of potential flow around obstacles of arbitrary shape. Bodies such as those addressed by Cheng and Liu [17] can be handled. A weighted residual derivation of the method for the solution of Laplace's equation is presented, and the inclusion of the appropriate boundary conditions at infinity considered. Computation of flow around a circular cylinder illustrates excellent agreement with the analytical solution and rapid convergence. Comparison with the boundary element results of Lesnic *et al.* [10] indicate that the new method obtains increased accuracy and more uniform convergence with increasing mesh density. The ability of the method to compute flow around shapes of practical importance is illustrated by application to the NACA 0012 wing section. Problems with singularities in the velocity field are handled accurately and efficiently by using bounded subdomains with the scaling centre located at the singular points. This approach is shown to accurately compute the flow around a square cylinder with very few elements. The application of substructuring techniques is illustrated by computation of the interaction between two square cylinders in uniform flow.

Overall the features of the scaled boundary finite-element method are shown to make it ideally suited to the analysis of potential flow around bluff and streamlined obstacles.

APPENDIX A: TRANSFORMATION TO THE SCALED BOUNDARY CO-ORDINATE SYSTEM

The scaling equations relating the Cartesian co-ordinate system to the scaled boundary co-ordinate system are

$$x = x_0 + \xi x_s(s) \tag{A1a}$$

$$y = y_0 + \xi y_s(s) \tag{A1b}$$

Derivatives in the scaled boundary co-ordinate system can be related to derivatives in the Cartesian co-ordinate system using the Jacobian matrix.

$$\begin{Bmatrix} \dfrac{\partial}{\partial \xi} \\ \dfrac{\partial}{\partial s} \end{Bmatrix} = \begin{bmatrix} \dfrac{\partial x}{\partial \xi} & \dfrac{\partial y}{\partial \xi} \\ \dfrac{\partial x}{\partial s} & \dfrac{\partial y}{\partial s} \end{bmatrix} \begin{Bmatrix} \dfrac{\partial}{\partial x} \\ \dfrac{\partial}{\partial y} \end{Bmatrix} \tag{A2}$$

Taking derivatives of Equations (A1) with respect to ξ and s separately, substituting into Equation (A2) and rearranging

$$\begin{Bmatrix} \dfrac{\partial}{\partial \xi} \\ \dfrac{1}{\xi}\dfrac{\partial}{\partial s} \end{Bmatrix} = \begin{bmatrix} x_s(s) & y_s(s) \\ x_s(s)_{,s} & y_s(s)_{,s} \end{bmatrix} \begin{Bmatrix} \dfrac{\partial}{\partial x} \\ \dfrac{\partial}{\partial y} \end{Bmatrix} \tag{A3}$$

Inverting yields

$$\begin{Bmatrix} \dfrac{\partial}{\partial x} \\ \dfrac{\partial}{\partial y} \end{Bmatrix} = \frac{1}{|J|} \begin{bmatrix} y_s(s)_{,s} & -y_s(s) \\ -x_s(s)_{,s} & x_s(s) \end{bmatrix} \begin{Bmatrix} \dfrac{\partial}{\partial \xi} \\ \dfrac{1}{\xi}\dfrac{\partial}{\partial s} \end{Bmatrix} \tag{A4}$$

where the Jacobian on the curve $S(\xi = 1)$ is

$$|J| = x_s(s) y_s(s)_{,s} - y_s(s) x_s(s)_{,s} \tag{A5}$$

and the incremental 'volume' is

$$\mathrm{d}\Omega = |J| \xi \, \mathrm{d}\xi \, \mathrm{d}s \tag{A6}$$

For convenience the operator ∇ is expressed as

$$\nabla = \mathbf{b}_1(s) \frac{\partial}{\partial \xi} + \mathbf{b}_2(s) \frac{1}{\xi} \frac{\partial}{\partial s} \tag{A7}$$

where, from Equation (A4),

$$\mathbf{b}_1 = \frac{1}{|J|} \begin{Bmatrix} y_s(s)_{,s} \\ -x_s(s)_{,s} \end{Bmatrix} \quad \text{and} \quad \mathbf{b}_2 = \frac{1}{|J|} \begin{Bmatrix} -y_s(s) \\ x_s(s) \end{Bmatrix} \tag{A8}$$

REFERENCES

1. Song Ch, Wolf JP. Consistent infinitesimal finite-element cell method: three-dimensional vector wave equation. *International Journal for Numerical Methods in Engineering* 1996; **39**:2189–2208.
2. Wolf JP, Song Ch. *Finite-Element Modelling of Unbounded Media*. Wiley: Chichester, 1996.
3. Song Ch, Wolf JP. Body loads in scaled boundary finite-element method. *Computational Methods in Applied Mechanical Engineering* 1999; **180**:117–135.
4. Song Ch, Wolf JP. The scaled boundary finite-element method—alias consistent infinitesimal finite-element cell method—for elastodynamics. *Computational Methods in Applied Mechanical Engineering* 1997; **147**:329–355.
5. Wolf JP, Song Ch. The scaled boundary finite-element method—a fundamental-solution-less boundary-element method. *Computational Methods in Applied Mechanical Engineering* 2001; **190**:5551–5568.
6. Deeks AJ, Wolf JP. A virtual work derivation of the scaled boundary finite-element method for elastostatics. *Computational Mechanics* 2002; **28**:489–504.
7. Deeks AJ, Wolf JP. Stress recovery and error estimation for the scaled boundary finite-element method. *International Journal for Numerical Methods in Engineering* 2002; **54**:557–583.
8. Song Ch, Wolf JP. Consistent infinitesimal finite-element cell method for diffusion equation in unbounded medium. *Computational Methods in Applied Mechanical Engineering* 1996; **132**:319–334.
9. Wolf JP, Song Ch. The scaled boundary finite-element method—a primer: derivations. *Computers and Structures* 2000; **78**:191–210.
10. Lesnic D, Elliot L, Ingham DB. Boundary element methods for determining fluid velocity in potential flow. *Engineering Analysis with Boundary Elements* 1993; **11**:203–213.
11. Lesnic D, Elliot L, Ingham DB. Treatment of singularities in exterior fluid domains with corners using the boundary element method. *Computers Fluids* 1994; **23**:817–827.
12. Zienkiewicz OC, Zhu JZ. The superconvergent patch recovery and a posteriori error estimates. Part 1: The recovery technique. *International Journal for Numerical Methods in Engineering* 1992; **33**:1331–1364.
13. Zienkiewicz OC, Zhu JZ. A simple error estimator and adaptive procedure for practical engineering analysis. *International Journal for Numerical Methods in Engineering* 1987; **24**:337–357.
14. Deeks AJ, Wolf JP. An *h*-hierarchical adaptive procedure for the scaled boundary finite-element method. *International Journal for Numerical Methods in Engineering* 2002; **54**:585–605.
15. Zienkiewicz OC. *The Finite Element Method.* (3rd edn). McGraw-Hill: London, 1977.
16. Selig M. http://www.uiuc.edu/ph/www/m-selig/ads/coord_database.html. *Airfoil co-ordinates database.* 2000.
17. Cheng M, Liu GR. Effect of afterbody shape on flow around prismatic cylinders. *Journal of Wind Engineering and Industrial Aerodynamics* 2000; **84**:181–196.

